Vortical Flow Structure in the Wake of an Estate Car

Phillip Gwo-Yan Huang[1] and Tony Wen-Hann Sheu[2,*]

[1] *Hon Hai Precision Ind. Co., Ltd., Taipei, Taiwan.*
[2] *Department of Engineering Science and Ocean Engineering, National Taiwan University, Taipei, Taiwan.*

Abstract. A finite volume simulation of unsteady vortical wake flow behind a square-back estate car is presented. The three-dimensional time-averaged incompressible Navier-Stokes equations are solved together with the Reynolds stress transport equations for turbulence. By virtue of the simulated surface streamlines, the physics of fluid can be extracted using the topological theory. In addition, the simulated topological singular points and lines of separation are plotted on the car surface. The vortical flow motions that developed behind the mirrors, wheels and car body are explored by means of the simulated time evolving vortex corelines. The formation and interaction of the vortex systems in the wake are examined by tracing the instantaneous streamlines in the vicinity of simulated vortex corelines. The vortex street behind the estate car is also illustrated by the simulated streaklines. Finally the Hopf bifurcation phenomenon is revealed by the time-varying aerodynamic forces on the car.

1 Introduction

Airflow around a vehicle can be physically very complex due to nonlinear nature of equations of motion. What further complicates the exterior aerodynamics is the variety of appendants on the car surface, which can strongly affect the car performance. For example, an aerodynamic designed wing mirror helps to gain 5% drag reduction for a typical diesel-engine heavy truck. The resulting fuel saving can be with an amount of 500-1000 liters a year. Besides improving fuel economy owing to drag reduction, issues such as the wind loading, handling of rain, snow and dirt around the vehicle are also crucial. Note

---

*Corresponding author. *Email addresses:* gwoyanhuang@gmail.com (P. G.-Y. Huang), twhsheu@ntu.edu.tw (T. W.-H. Sheu)

that cabin ventilation, underhood thermal management and brake cooling depend also on the external aerodynamics. To meet the desired vehicle aerodynamic design requirements, there is a strong need for acquiring more information about the air flow behavior around vehicle.

In the past, wind tunnel testing is the sole source to obtain aerodynamic data around the vehicle. With the advent of increasingly faster and cheaper high-performance computers and commercially available codes for grid generation and flow visualization, the flow details around automobiles can be obtained cost-effectively by means of flow simulation. The simulated results can be correlated with test results to within 5%, while temperatures correlated to within 10%. Nowadays, the numerical simulation tool has been the daily practice in the vehicle design. Almost all the major automobile manufactures combine now the capabilities of wind tunnel testing and computational fluid dynamics techniques and put them to optimal use for obtaining a best designed vehicle shape [1–3].

The rest of this paper is organized as follows. In Section 2 working equations for incompressible viscous fluid flow, transport equations for Reynolds stresses, boundary conditions and aerodynamic force equation are described for use in external car aerodynamics. This is followed by brief descriptions of the packages Pro/Engineer [4], ICEM-CFD [5], CFX [6] and FIELDVIEW [7] for CAD, mesh generation, flow solver and visualization of simulated results, respectively, in Section 3. In Section 4, results are presented in addressing flow topology, formation of vortex corelines, and field variables such as pressure distribution, velocity vectors, streamlines, streaklines, and time-varying aerodynamic forces. Finally, conclusions are drawn in Section 5.

2 Model equations

Airflow over the investigated car schematic in Fig. 1 is unsteady and turbulent in nature. We, therefore, need to solve for the transient incompressible Navier-Stokes equations together with the Reynolds stress transport equations to account for turbulence.

Figure 1: The full model for the investigated estate car, namely, the Mitsubishi Freeca. Photograph courtesy of China Motor Car.

The employed differential stress turbulence model [8, 9], which deals with the transport equations of the Reynolds stress components and dissipation rates, should be suitable for modelling an anisotropic swirling flow around a vehicle [10].

2.1 Governing equations

The continuity and momentum equations for the incompressible fluid flow with the molecular viscosity μ can be described as

$$\frac{\partial \rho}{\partial t} + \nabla \cdot (\rho \mathbf{U}) = 0, \tag{2.1}$$

$$\frac{\partial \rho \mathbf{U}}{\partial t} + \nabla \cdot (\rho \mathbf{U} \otimes \mathbf{U}) - \nabla \cdot (\mu (\nabla \mathbf{U} + (\nabla \mathbf{U})^T)) = -\nabla p' - \nabla \cdot (\rho \overline{\mathbf{u} \otimes \mathbf{u}}). \tag{2.2}$$

In the above, ρ and $\mathbf{U} = (U, V, W)$ denote the mean fluid density and flow velocity. Note that p' is the modified pressure defined by

$$p' = p + \left(\frac{2}{3}\mu - \zeta\right) \nabla \cdot \mathbf{U}. \tag{2.3}$$

On the right hand side of Eq. (2.3), p is the static pressure and ζ is known as the bulk viscosity.

In the differential stress model, the Reynolds stress components in Eq. (2.2) are governed by the following transport equation

$$\frac{\partial \rho \overline{\mathbf{u} \otimes \mathbf{u}}}{\partial t} + \nabla \cdot (\rho \mathbf{U} \otimes \overline{\mathbf{u} \otimes \mathbf{u}}) - \nabla \cdot \left(\left(\mu + \frac{2}{3} C_s \rho \frac{k^2}{\varepsilon} \right) \nabla \overline{\mathbf{u} \otimes \mathbf{u}} \right)$$

$$= \mathbf{P} + \varphi - \frac{2}{3} \rho \varepsilon \delta. \tag{2.4}$$

Here, $\mathbf{P}$ is the shear production and is given by

$$\mathbf{P} = -\rho \left(\overline{\mathbf{u} \otimes \mathbf{u}} (\nabla \mathbf{U})^T + (\nabla \mathbf{U}) \overline{\mathbf{u} \otimes \mathbf{u}} \right). \tag{2.5}$$

As for the pressure-strain correlation term φ, it is defined by

$$\varphi = -\rho \varepsilon \left(C_{\varepsilon 1} a + C_{\varepsilon 2} \left(aa - \frac{1}{3} a \cdot a \delta \right) \right) - C_{r1} P a + C_{r2} \rho k S - C_{r3} \rho k S \sqrt{a \cdot a}$$

$$+ C_{r4} \rho k \left(aS^T + Sa^T - \frac{2}{3} a \cdot S \delta \right) + C_{r5} \rho k (a\omega^T + \omega a^T), \tag{2.6}$$

where

$$a = \frac{\overline{\mathbf{u} \otimes \mathbf{u}}}{k} - \frac{2}{3}\delta, \tag{2.7}$$

$$S = \frac{1}{2} (\nabla \mathbf{U} + (\nabla \mathbf{U})^T), \tag{2.8}$$

$$\omega = -\frac{1}{2} (\nabla \mathbf{U} - (\nabla \mathbf{U})^T). \tag{2.9}$$

In the above, a is the anisotropy tensor, S the strain rate and ω the vorticity. The turbulent kinetic energy k can be calculated from

$$k = \frac{1}{2}\overline{\mathbf{u}^2}. \tag{2.10}$$

The turbulence dissipation rate ε is governed by the following transport equation

$$\frac{\partial \rho \varepsilon}{\partial t} + \nabla \cdot (\rho \mathbf{U} \varepsilon) - \nabla \cdot \left(\frac{1}{\sigma_{\varepsilon RS}} \left(\mu + \rho C_{\mu RS} \frac{k^2}{\varepsilon} \right) \nabla \cdot \varepsilon \right)$$
$$= \frac{\varepsilon}{k} (C_{\varepsilon 1} P - C_{\varepsilon 2} \rho \varepsilon). \tag{2.11}$$

Referring to Launder et al. [8], the empirical constants used in the employed turbulence model are chosen as $C_{\mu RS} = 0.1152$, $\sigma_{\mu RS} = 1.10$, $C_s = 0.22$, $C_{\varepsilon 1} = 1.45$, $C_{\varepsilon 2} = 1.9$, $C_{s1} = 1.8$, $C_{s2} = 0.0$, $C_{r1} = 0.0$, $C_{r2} = 0.8$, $C_{r3} = 0.0$, $C_{r4} = 0.6$, $C_{r5} = 0.6$.

2.2 Boundary conditions

The physical domain containing the car and the wind tunnel to be investigated is represented in Fig. 2. At the entry plane, air flow with a velocity value of 110 km/h is prescribed. The no-slip condition was applied on the car surface, mirrors, wheels and the ground. The surrounding far-field boundaries are supplemented with the free slip condition. At the truncated downstream boundary plane, it is prescribed with the zero static pressure. The Reynolds number is obtained as $Re = 8.05 \times 10^6$ based on the air speed, length of the model car (4.43 m) and the dynamic viscosity of the air at 25°C.
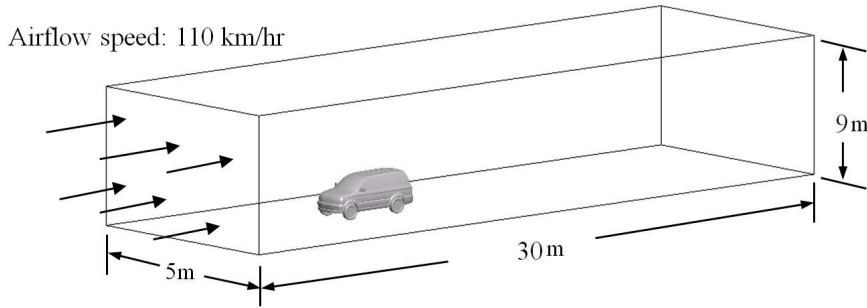

Figure 2: The CAD model which represents the physical domain containing the car to be investigated.

2.3 Aerodynamic force equation

The forces that the external airflow exerts on the car body (often called aerodynamic forces) are of interest to engineers. The net force on the car body can be calculated by

integrating the static pressure (p) and shear stress (τ_w) over the surface:

$$\overrightarrow{F} = -\oint p\hat{n}dA + \oint \tau_w\hat{t}dA, \tag{2.12}$$

where $\hat{n}$ and $\hat{t}$ are unit vectors normal and tangent to the car surface. The first term in the right side of Eq. (2.12) is called pressure force and the second is called viscous force. As shown in Fig. 3, the aerodynamic forces on the car body can be broken into components along any set of axes. The force component in the direction of the approaching flow (X-direction in this study) is called drag. Drag resists the motion of the car. The force component perpendicular to the approaching flow and horizontal to the ground (Y-direction in this study) is called side force. Side force tends to move the car right or left. The force component perpendicular to the approaching flow and vertical to the ground is called lift (Z-direction in this study). Lift force may lift the car. However, the driver is generally unaware of lift at ordinary highway speeds, as long as the weight of the car is greater than the lift.
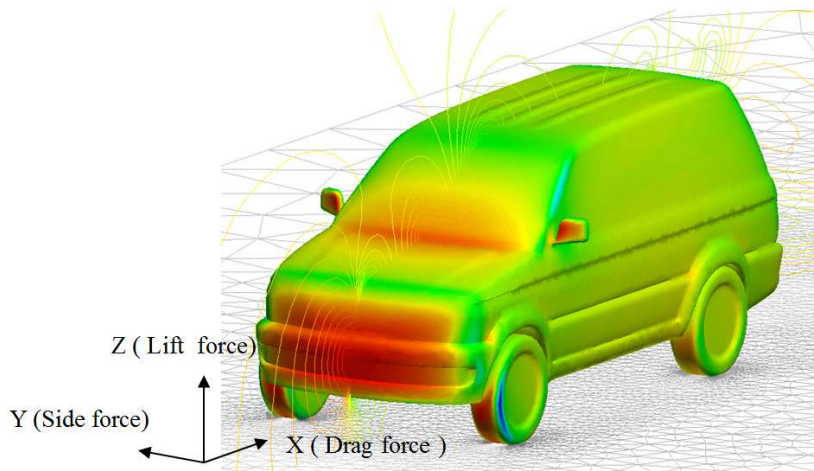

Figure 3: A schematic plot of the aerodynamic forces on the three-dimensional car body. The net force has three components, called drag, lift, and side force.

3 Numerical modelling

Simulation of an estate car, known as the Mitsubishi Freeca, starts with the surface pre-processing. This is followed by generating computational grids, conducting analysis of the governing equations and, then, the visualization of the simulated results. The four major simulation phases are briefly described below. Firstly, the CAD shell data for the investigated Freeca is provided by China Motor car manufactures, from which vehicle parts and components can be integrated and meshed to render a generic model schematic in
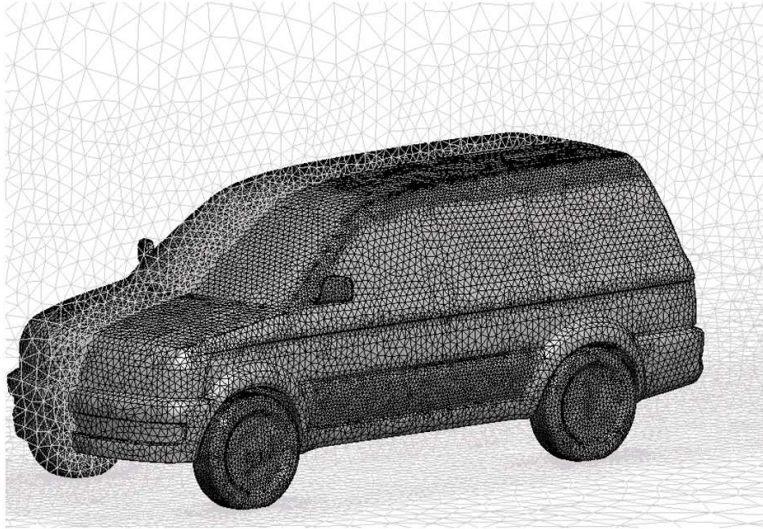
Figure 4: The generated grids on the car surface, the longitudinal central plane and the ground.

Fig. 1. The software package used in the CAD step is the Pro/Engineer [4]. Subsequent to the integration, preparation and clean-up of the Pro/E-generated CAD model illustrated in Fig. 2, the surface grid generation is made by exporting the CAD data in a native geometry format of the grid generation system ICEM-CFD [5]. The shaded surface grid is schematic in Fig. 4. Note that the non-uniform surface grids are seen in regions having a sharply varying geometry and in near wall regions for resolving flow details.

With the surface grid that was generated by ICEM-CFD, we can now discretize the physical domain bounded by the wind tunnel and the car body. Our tool is applied to generate tetrahedral grids, which are useful for resolving boundary layers over the car body. A key aspect of the current full model grid generation is the use of mirror imaging of grids generated in a half model accommodated with a symmetry plane. This helps to avoid asymmetrically generated grids in the geometrically symmetric domain. The simulated asymmetric flow nature, if any, can then be attributed to the bifurcating solution owing to the equation nonlinearity.

Within the three dimensional context, the time-dependent, incompressible Navier-Stokes equations are solved together with the divergence-free constraint equation using the unstructured finite-volume code CFX. In co-located grids, the Rhie-Chow interpolation [11] is applied to avoid oscillating values of $(\mathbf{U}, p)$ due to even-odd coupling. As an another major issue that can contaminate the present flow simulation due to lack of sufficient grids, the turbulence model is considered indispensably. For this reason, we employ a computationally more expensive but physically more rigorous Reynolds stress model described in Section 2.

Therefore, this numerical approach involves discretization of the integral form of the Navier-Stokes and the Reynolds transport equations, which are solved over a number of

volumes within the fluid domain. When solving these continuous equations numerically, the first step is to approximate them to their discrete counterparts. For the discretization of the convection term, it is physically reasonable to approximate it using the upstream nodal values, as transported variables move with the flow. This approximation involves series expansion, and is called the upwind-difference scheme [12]. The first-order accurate upwind-difference scheme is usually very robust. However, this scheme can be susceptible to large numerical diffusion error. For the sake of reducing numerical diffusion, the second-order upwind-difference scheme is used to approximate the convection terms, while the diffusion term is discretized using a centered difference scheme.

For this transient-state problem, a robust fully implicit backward time-stepping scheme [13] is adopted for the temporal derivative term. This solution process consists of two numerically intensive operations. For each timestep, the non-linear equations are linearised firstly, then the linear equations are solved subsequently. In this transient analyses, a small time step Δt=0.005 s is used to achieve convergence. Besides, the discrete system of linearised equations is solved using an iterative algebraic multigrid solver [14]. The process of multigridding involves carrying out iterations on a fine mesh firstly and later iterations on its progressively coarser virtual ones. The results are then transferred back from the coarsest mesh to the original fine mesh. The equations shall be solved exactly in the coarsest grid. Finally, we can visualize the simulated results by virtue of the post-processor FIELDVIEW [7] to obtain some significant physical insights.

Airflow around a vehicle usually exhibits vortical flow characteristics that are similar to those seen around a wall-mounted obstacle. However, a much more complex flow pattern can be seen around the car body because of the additional geometrical complexity due to fenders, bonnet, windscreen, mirrors, wheels, wheel wells, underfloor, trunk, etc. Inevitably, there also exist many turning and angular deformations around the car surface. Therefore, the vortical flow motion around the vehicle is less fully understood. Much of the recent effort has been made for gaining a full understanding of this subject. As CAD and CAE have come to play an increasingly dominant role in the exploration of flow details around a moving vehicle, in the literature there exist numerical studies of vortical flows around vehicles with notch-back or fast-back configurations [15, 16]. The simulated wake pattern behind the vehicle was found to contain several longitudinal vortex pairs. Typical of them are the horseshoe vortex on the cowl top, arch-type vortex behind the rear window, and trailing vortex behind the trunk.

In this study, airflow around an estate car with a sloping square-back is investigated numerically. Our objective is to reveal vortex formation mechanism and its development in the wake region. In order to analyze the unsteady vortical flow, a transient calculation is performed to gain the insight of the resulting vortical flow by means of the topological theory. Plots such as the streamlines, velocity vectors, and pressure distribution are considered useful to understand the formation and interaction of the vortex systems (arch-type, uptilting and the long trailing vortex). Furthermore, the vortex street in the wake is revealed by the simulated streaklines. Finally, the Hopf bifurcation [17] is revealed as well by the time-varying aerodynamic forces acting on the car.

4   Results and discussion

External flow over a sloping square -back estate car is simulated. The present simulation involves wheels, wheel wells, underfloor, mirrors, smooth corners, rounded edges, rooftop air deflectors, as shown in Fig. 1. Both air-cooling vents and engine space above the car underfloor are assumed to be closed so as to simplify the analysis. In this study, the car is simulated in a rectangular domain, schematic in Fig. 2, with a dimension that is 2 times of the car body length upstream, 5 times downstream, 7 times of the width sideward, and 5 times of the height upward, respectively. These chosen lengths are appropriate in a sense that the influence of free stream boundaries on the computed flow is negligibly small.

4.1   Grid density test

In order to maintain adequate resolution of the interior flow field, the computational grid density test is performed first. Fig. 5 illustrates the effect of grids on the simulated accuracy of pressure drag force at time t=1.0 s. The minimum allowable number of grids to obtain the grid-independent pressure drag is found to exceed 1.5 million. The volumetric grids, schematic in Fig. 4 with 1.68 million cells, are then exported into CFX [6] and the pre-processing is completed.
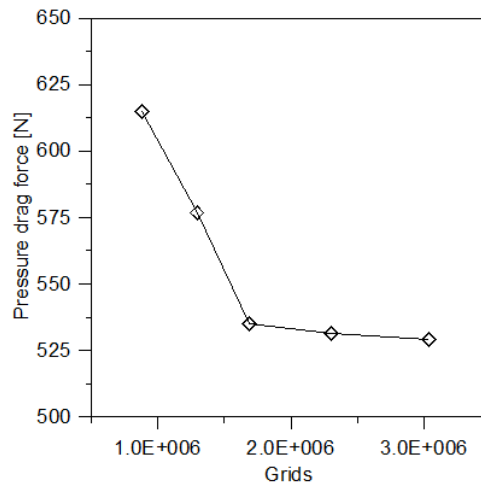

Figure 5: Effect of grids on the simulated accuracy of pressure drag force at t=1.0 s.

4.2   Flow topology

The present study aims to reveal flow details by conducting a topological study of the surface streamlines. A streamline is an imaginary line that is everywhere tangent to the fluid velocity vector. The streamline immediately above the wall is called wall limiting

streamline or surface streamline. The flow topology on the car surface is revealed by plotting in Figs. 6(a) and 6(b) the surface streamlines, which are color-coded with the magnitude of wall shear stresses at t=0.2 s.

The arrows on these surface streamlines indicate their flow directions. The limiting streamlines on the car surface are highly curved due to the non-planar car shape. The topologically singular points of separation, labelled with F, N and S, are referred to as the spiraling focus, nodal attachment node, and saddle attachment point, respectively. At the saddle attachment point (S), the surface streamlines approach or repel. The place where all neighboring streamlines pass through and fluid particles split or branch is called a nodal attachment node (N). The attachment point where the streamlines spirally approach without having a common tangent is called the spiraling focus (F). At these critical points, the wall shear stress is zero. Furthermore, owing to the smoothly varying edges of the car, the lines of separation are seen to occur at the rear-end of the car surface. Note that no such lines were observed in the wake of a wall-mounted rectangular block [18].

4.3   Time-evolving vortex corelines

Fig. 7 presents the vortex corelines colored by vortex strength (the magnitude of vorticity, unit:1/s) in the wake, in addition to the surface streamlines (red lines). The vortex corelines represent axes of swirl in regions of high vorticity. In this study, the vortex cores are calculated based on the eigenmode analysis [19,20]. The vortex cores are clipped into line segments. Note that the portions where the value of vortex strength is small are clipped.

As shown in Fig. 7, three typical counter-rotating vortex pairs denoted by $A(A_L,A_R)$, $B(B_L,B_R)$, $C(C_L,C_R)$ are seen. They are known as the arch-type vortex, uptilting vortex, and the trailing vortex pairs, which are generated in regions near the rear window, rear fender, and rear-side pillars, respectively. These vortices are seen to originate from the spiral foci. The arrows represent the directions of spiraling fluid particles in the vicinity of the vortex corelines. Due to the underlying unsteady nature, their appearance depends on the car speed. For example, Fig. 7 is an instantaneous pattern at time t=0.2 s for the car moving at a speed of 110 km/h. In general, this vortical pattern is typically seen behind the estate car.

Figs. 8(a) to 8(e) depict the vortical flow patterns around the car at a time in between t=0.2 s and t=1.0 s. The red lines on the car surface are the wall limiting streamlines. The vortex corelines color-coded with the vortex strength (unit:1/s) are illustrated in the wake of the mirrors, wheels, and the car body.

In the course of flow development, a large portion of flow domain is seen to maintain at a quasi-steady state near the region upstream of the car, while the downstream wake flow behind the mirrors, wheels, and rear-end of car body exhibits unsteady characteristics. The air viscosity is significant only in the thin region that is immediately adjacent to the wall. The vortex corelines, proceeding downstream with time, undergo dissipation, cross-cancellation or somehow merge with other vortices, thus contributing to the
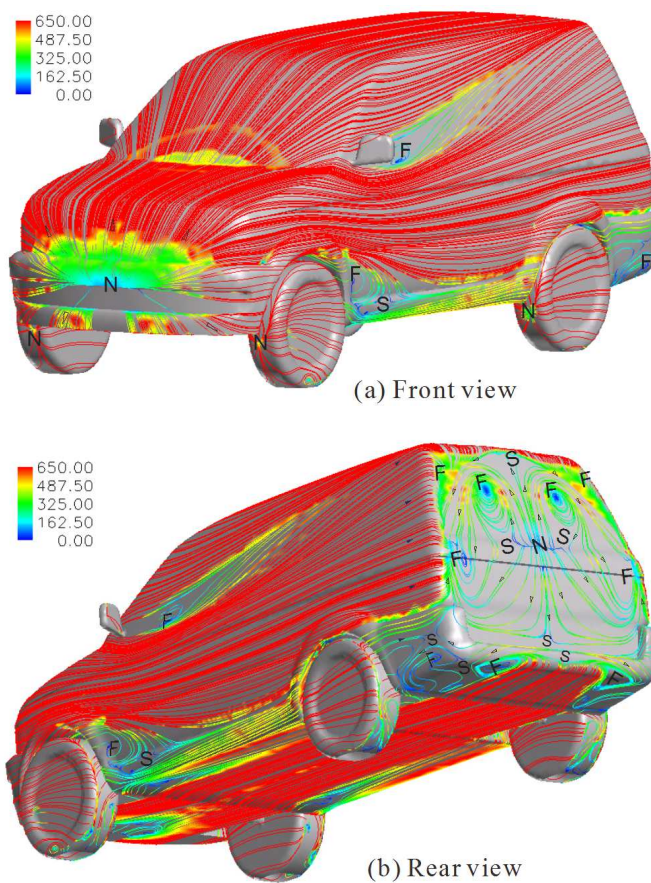
(a) Front view

(b) Rear view

Figure 6: The simulated surface flow topology at (a) front view and (b) rear view, at time t=0.2 s. The surface streamlines are color-coded with the simulated wall shear stresses (unit:N/m^2). The topologically singular points of separation, labelled with F, N and S, are referred to as the spiraling focus, nodal attachment node, and saddle attachment point, respectively. At these critical points, the wall shear stress is zero.
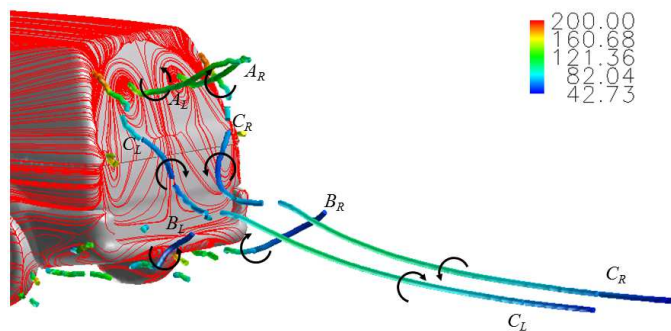

Figure 7: Three main vortex systems, denoted by $A(A_L,A_R)$, $B(B_L,B_R)$, and $C(C_L,C_R)$, which correspond to the arch-type vortex, uptilting vortex, and trailing vortex. They are generated near the rear window, rear fender, and rear-side pillars, respectively, at t=0.2 s. The arrows represent the directions of spiraling fluid particles in the vicinity of the vortex corelines.
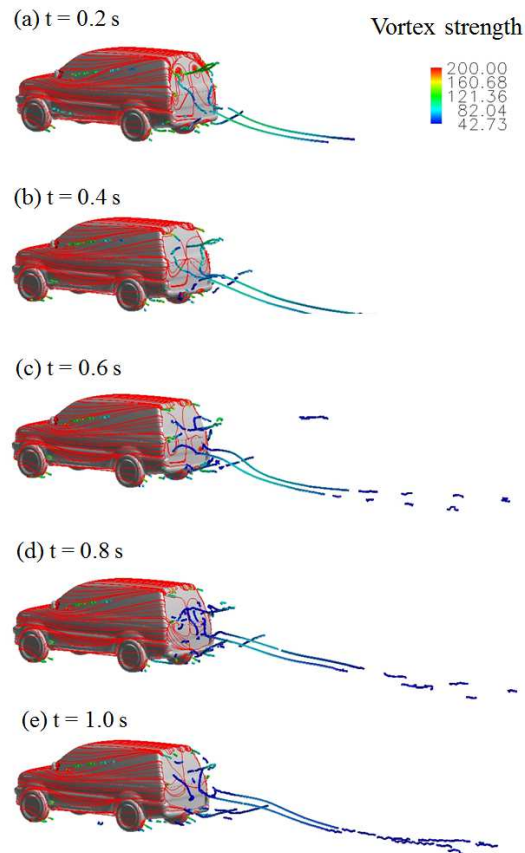
(a) t = 0.2 s

Vortex strength

```
200.00
160.68
121.36
82.04
42.73
```

(b) t = 0.4 s

(c) t = 0.6 s

(d) t = 0.8 s

(e) t = 1.0 s

Figure 8: The time-evolving vortex corelines color-coded with the vortex strength (unit:1/s) obtained in between t=0.2 s and t=1.0 s. These vortex corelines represent axes of swirl in regions of high vorticity.

wake development. These corelines prevail near the car surface where the vortices are generated. They become weaker at the downstream side. The vortices are, however, strengthened at the location where two streams of fluids meet together.

At t=0.2 s (Fig. 8(a) and Fig. 7), the flow pattern remains quite symmetric. At the very inception of vortex A (or the arch-type vortex), a pair of foci is seen on the rear window near the downstream end of the roof. Vortex C (or the trailing vortex) emanates from the rear-side pillars and extends itself downstream. These two vortex pairs can jointly cause a downwash flow to occur. Vortex B (or the uptilting vortex) originated below the rear fender, on the other hand, induces an upwash flow. Vortex B is seen to lift, tilt and, eventually, merged with vortex C. The range of vortex B is less affected than those for A and C.

As time proceeds (Figs. 8(b) to 8(e)), the oncoming flow interacts with the car surface and can cause the time-varying topological singular points and lines to occur on the rear-end of the car surface. Several spiraling foci along the roof end, rear window, rear-side

pillars and rear fender are seen to induce some new streamwise vortices. The vortex core-lines are all periodic in elongation, followed by a split-off tail due to vorticity production and cross-cancellation. The split tail of vortex B terminates its development when connecting the vortex C. Vortex C trails further downstream and its segment spreads over the ground. The wake size, therefore, becomes enlarged. Note that the flow will continue to lose symmetry due to interaction between the counter-rotating vortices and the subsequent merger of different vortex systems.

4.4   Streamlines and pressure distribution

A more detailed characteristic of the longitudinal vortex system in the wake is discussed. Fig. 9 illustrates the wall surface streamlines (red lines on the car surface) and the streamlines in the flow field at t=0.2 s. The streamlines in green color represent the vortex A, yellow for the vortex B, light blue for the vortex C, and blue for the peripheral airflow.
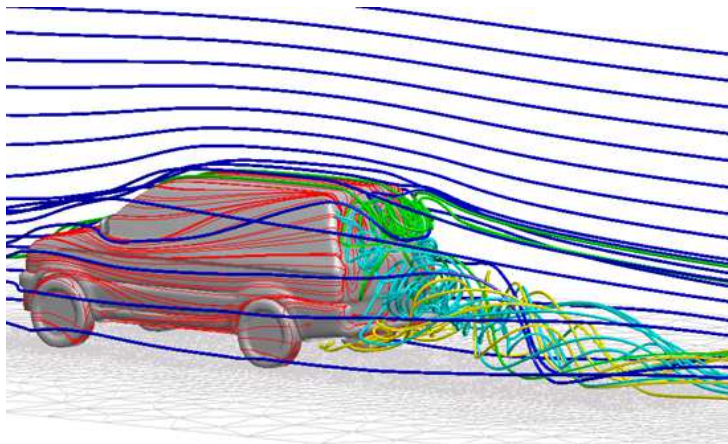

Figure 9: The simulated surface streamlines (red lines) and the streamlines over the car (green for vortex A, yellow for vortex B, light blue for vortex C, and blue for the peripheral airflow) at t=0.2 s.

The airflow is seen to separate from the rear-end of the car surface. The streamlines are spirally configured and form several three-dimensional recirculation eddies in the wake. Moreover, it can be seen from this figure that part of the upstream streamlines for vortex A and most of the streamlines for vortex B are entrained into the vortex C. Vortex C is enhanced at the place where it is merged with the other two primary vortex systems, as indicated in Fig. 8(a).

Figs. 10 and 11 show the relative pressure distributions on the car surface, ground, streamlines and the longitudinal central plane at t=0.2 s. In the wake region, the vortex core is seen to consist of a low pressure region. The pressure gradient becomes increasingly apparent in the approach to the vortex cores.

Fig. 12 on the other hand presents the pressure distribution on the surface streamlines and vortex corelines. It can be seen from this figure that the pressures are high in the re-
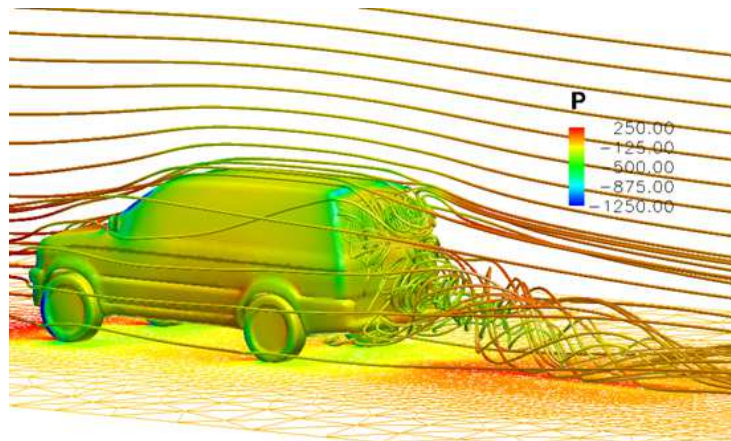
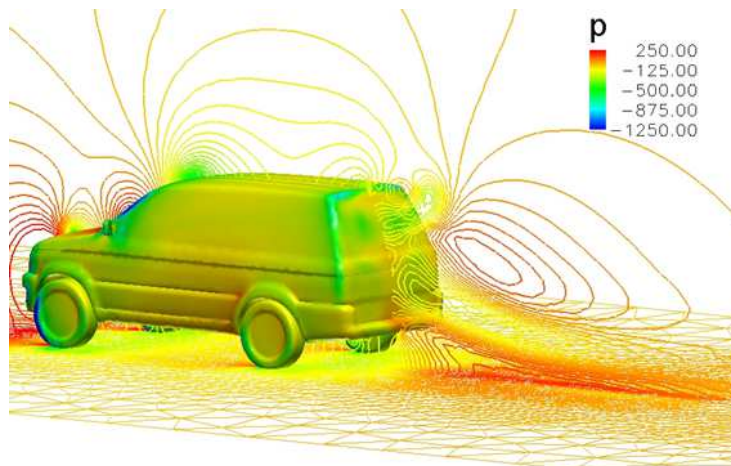Figure 10: The simulated relative pressure distributions on the car surface, ground, and streamlines at t=0.2 s.

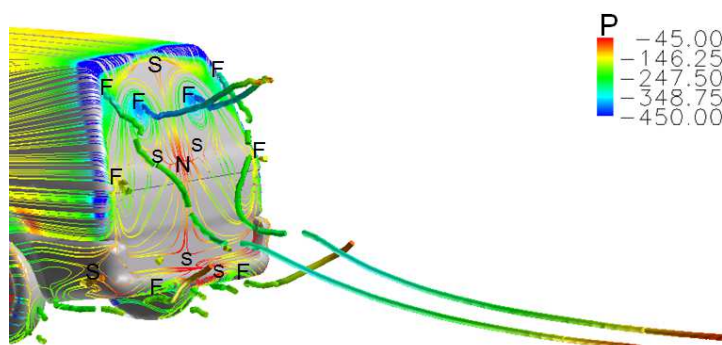Figure 11: The relative pressure contours on the car surface, ground, and longitudinal central plane at t=0.2 s.

Figure 12: The relative pressure distribution on the surface streamlines and vortex corelines at t=0.2 s.

gions near the noddle attachment node (N) and saddle attachment point (S). The spiraling foci (F) where the vortex corelines are originated, however, have low pressures. Furthermore, following the vortex coreline, it can be observed that the pressure is lower in the region near the spiraling focus and the place where different vortices merge together. The pressure is, on the contrary, getting larger on the way to the tail of the coreline. It is noted that the fluid particles have a tendency to be converged in the low pressure region and diverged in the region where the pressure is high, as can be seen from Fig. 10.

Figs. 13(a) to 13(c) reveal the instantaneous streamlines in the vicinity of vortex corelines (purple lines) for A_L, B_L, and C_L, respectively, at time t=0.2 s. It is noted that at this moment the flow patten is nearly symmetric with the longitudinal central plane. Thus, we only discuss the flow behavior in one half of the vortex system. As observed in these figures, there are some spiraling foci formed behind the rear-end of the car surface. Most likely, flow separation from all surfaces originates from these spiralling foci and takes place in a form of spiraling motion around the vortex corelines.

The formation mechanism of vortex A is shown in Fig. 13(a). Such an arch-type vortex is seen to originate from the spiraling foci on the rear window. The fluid particle along
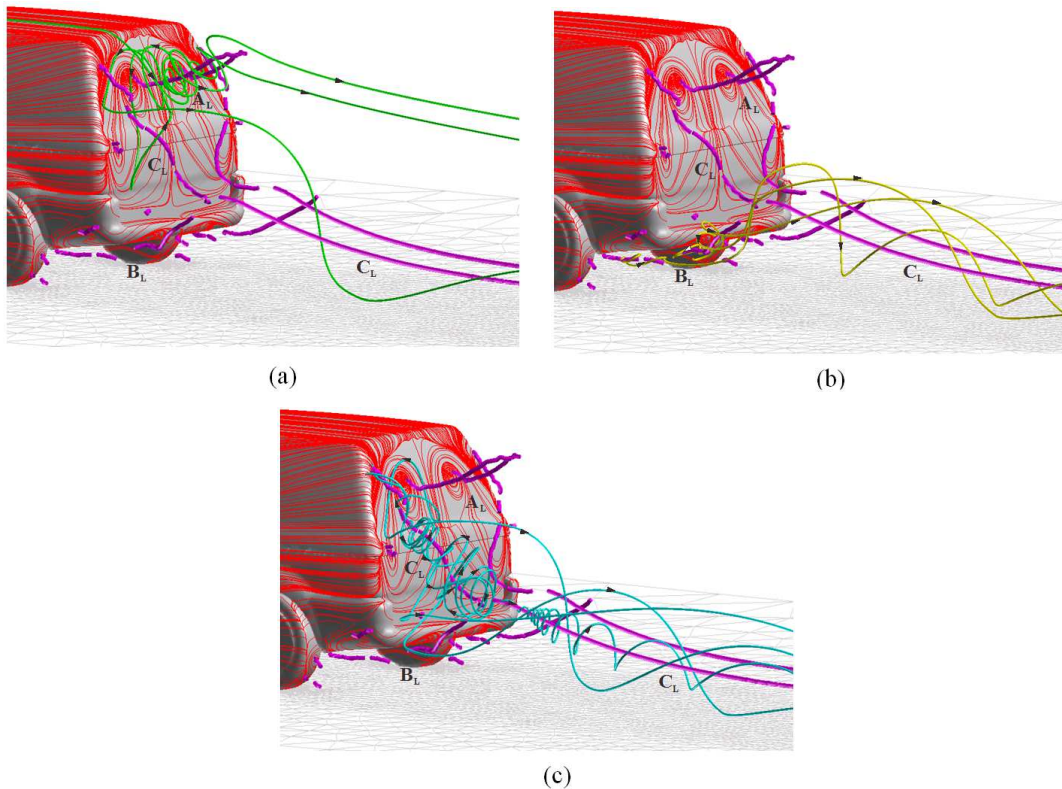

(a)

(b)

(c)

Figure 13: The instantaneous streamlines in the vicinity of (a) the arch-type vortex A_L; (b) the uptilting-type vortex B_L; and (c) the trailing-type vortex C_L at t=0.2 s.

the instantaneous streamline in the vicinity of vortex A_L proceeds upward or downward. The presence of upward moving fluid particles is the result of adverse pressure gradient established at the downstream side, as depicted in Figs. 10 and 11. There is a separation bubble, inside of which the fluid particles recirculate. As illustrated in Fig. 13(a), some upstream moving fluid particles merge and wrap around the vortex C_L. On the other hand, some particles sweep downstream continuously.

Fig. 13(b) shows the formation mechanism for vortex B. The vortex corelines for B are originated from the foci under the rear fender. Airflow coming from the underside of the car is swirling in nature around the vortex B_L, lifted up, and is gradually entrained into the vortex C_L, thus forming an uptilting vortex. Airflow under the rear fender is particularly unclear. As denoted in Fig. 6(b), there are several singular points of the separation on the rear fender. The saddle attachment points on the center of the rear fender represent the locally prevailing airflow. Therefore, vortex B induces an upwash wake flow and is responsible for the dust contamination seen in the rear of the car.

The formation of another primary wake vortex C, as shown in Fig. 13(c), is the result of a trailing-type counter-rotating vortex pair that emanates from the foci near the rear-side pillar. The flow direction illustrated in Fig. 7 has a tendency to recirculate along the upper and middle sides of the vortex coreline C_L owing to the presence of separation bubbles. The fluid particles along the streamlines in the vicinity of upper and middle portions of this coreline are spiraling, recirculating and, finally, trailing downstream. Vortex C gets strengthened owing to the momenta that vortices A and B provide and gradually becomes dominating in the streamwise direction.

4.5 Velocity field

Figs. 14(a) to 14(e) illustrate the three-dimensional flow velocity vectors, color-coded with the magnitude of velocity component U (unit: m/s), on several transverse test planes in the wake of the investigated estate car at t=0.2 s. These vector diagrams clearly reveal the truly three-dimensional wake vortices. It can be seen that the adjacent vortices rotate in an opposite direction. The trailing vortices of C are gradually merged with other vortices in the flow direction and wandered towards the ground. Its strength is slowly diminished along the downstream direction by means of dissipation.

As shown in Fig. 14(a), at X=3.70 m a plane immediately behind the rear end of the car, vortex A, B and C are seen to form by their corresponding counter-rotating vortex pairs. Some of the fluids with the negative value of U recirculate and move upstream. At X=4.10 m (Fig. 14(b)), the uptilting vortex B merged with vortex C. At X=4.40 m (Fig. 14(c)), the arch-type vortex A is merged with the vortex C and form a strong interaction amongst vortices. The vortex C is strengthened and exhibits a clear counter-rotating vortex pair. At a further downstream location (Fig. 14(d)) at X=6.00 m, only the trailing vortex remains visible and all fluids move downstream. The strength of the vortex decreases due to the dissipation effect. Finally, at the plane X=8.50 m (Fig. 14(e)), the vortices disappear entirely and the fluids move downstream.
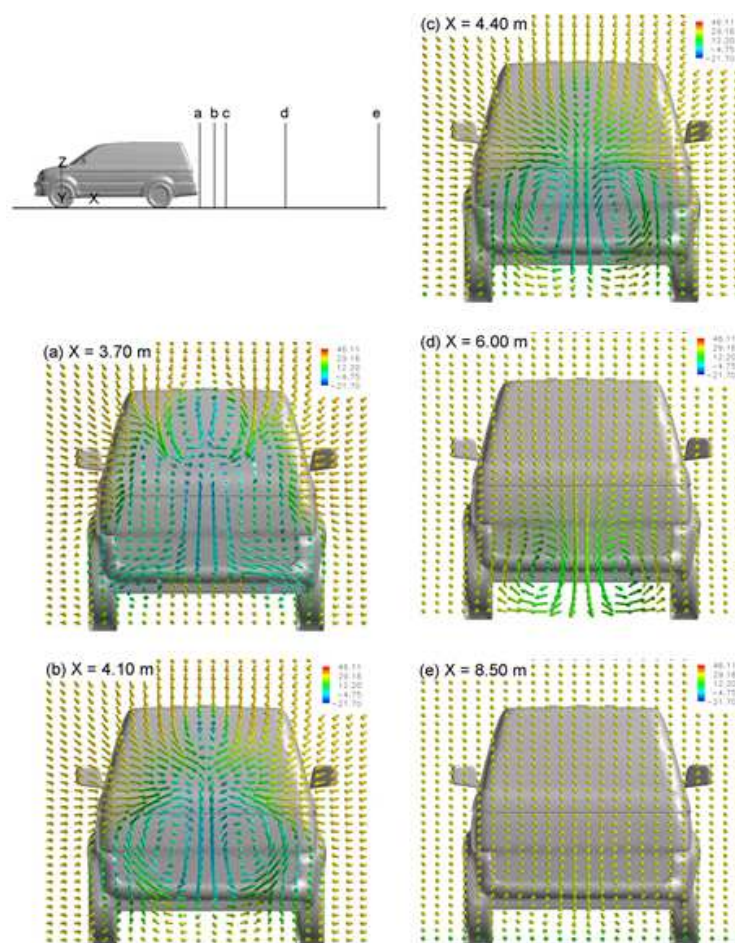
Figure 14: The simulated three-dimensional flow velocity vectors, color-coded with the magnitude of velocity component U (unit: m/s), on several chosen transverse test planes in the wake of the estate car at t=0.2 s.

4.6   Simulated streaklines

For a good understanding of the transient turbulent flow nature, the animated streaklines are employed to visualize the evolving particle streams by tracing the seeded particles. A streakline is a line composed of fluid particles. It's made up of all particles that have passed a certain point. Figs. 15(a) to 15(g) show the particle streaklines from t=0.05 s to t=1.0 s. At t=0.05 s, some fluid particles are emitted from a region near the rear-end of the car surface. As time goes by, some particles recirculate in the wake and even collide with the car rear-end. The other particles move downstream spirally, as shown in Figs. 15(b) to 15(d). The vortices are generated periodically and shed away from the car. Their tails sweep and propagate downstream until they disappear at the ground. As can be seen from Figs. 15(e) to 15(g), the vortex street is, thereafter, confirmed to show its appearance in the wake.
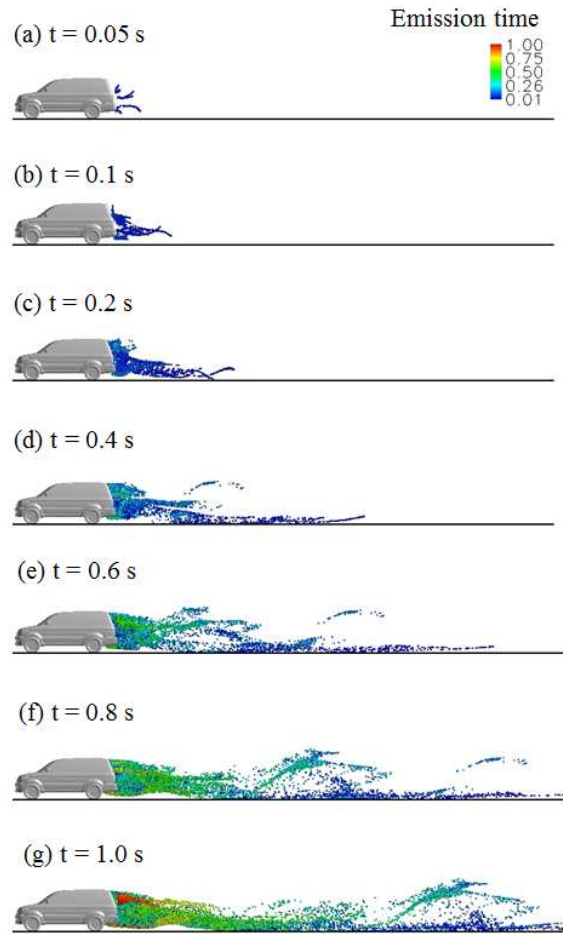
(a) t = 0.05 s

Emission time

(b) t = 0.1 s

(c) t = 0.2 s

(d) t = 0.4 s

(e) t = 0.6 s

(f) t = 0.8 s

(g) t = 1.0 s

Figure 15: The simulated particle streaklines from t=0.05 s to t=1.0 s. Each particle is color-coded with its emission time (unit: s).

4.7 Time-varying aerodynamic forces

Fig. 16 presents the calculated aerodynamic forces defined in Section 2.3. According to the force-time history profiles, all the force components are periodically varying with time. Especially is the side force whose sign is appeared to be alternatively changed with time. It means that the side force direction is varied with time and tends to move the car right or left. These time-varying loads are caused by the fluctuating forces on the car which are originated from the oscillating flow pattern caused by the alternate vortex shedding, as discussed in Section 4.6. This oscillating phenomenon can be taken as a type of Hopf bifurcation [17].

Furthermore, a comparison of the pressure force (Figs. 16(a) to 16(c)) and the viscous force (Figs. 16(d) to 16(f)) reveals that the pressure force is about 10^2 greater than
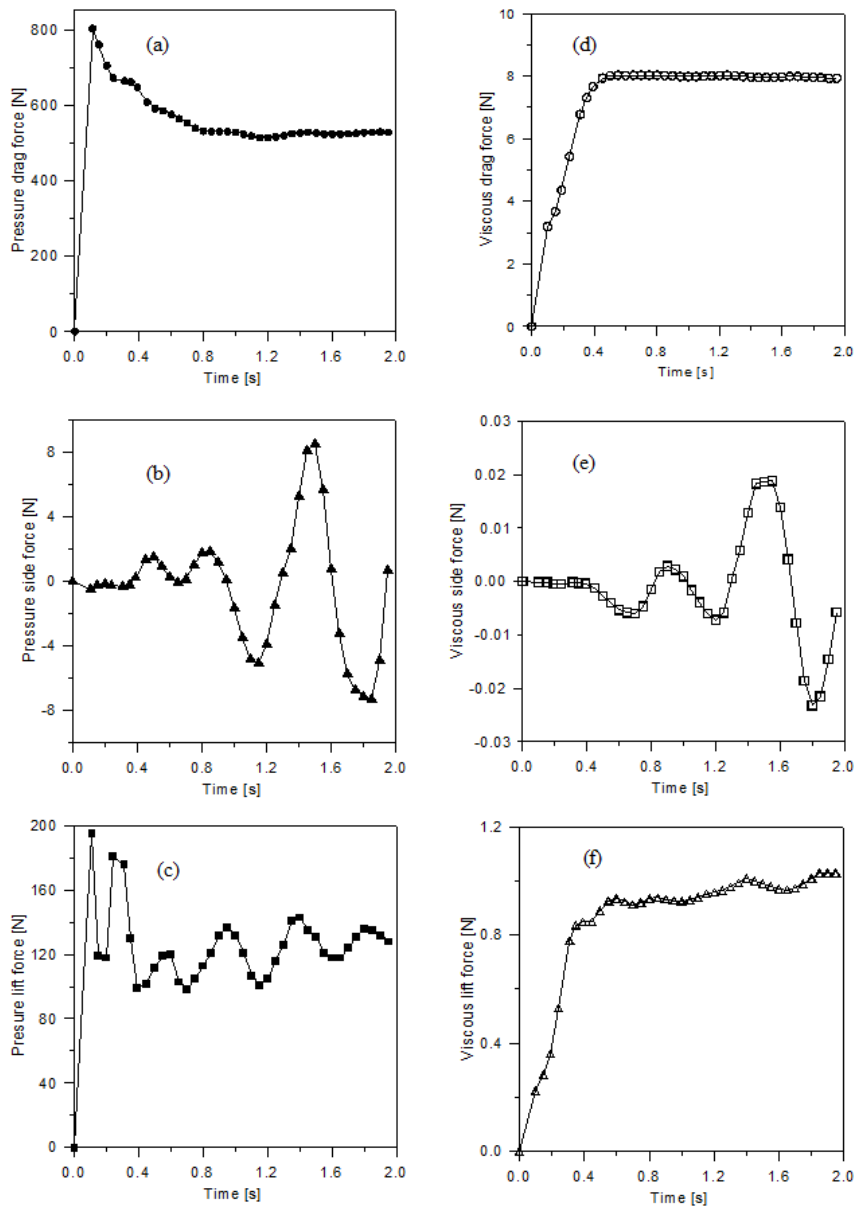
Figure 16: The time-varying profiles of (a) pressure drag, (b) pressure side, (c) pressure lift, (d) viscous drag, (e) viscous side and (f) viscous lift forces on the car body.

the viscous force. In addition, this comparison also depicts that the pressure drag force (Fig. 16(a)) which varies between 515N and 535N is obviously greater than the other components. Therefore the aerodynamic force on the car body is dominated by the pressure drag or form drag. There are many possible methods applicable to reduce the form drag, such as surface streamlining or the installation of rear wing and spoiler.

5 Conclusions

The vortical flow around the square-back estate car, namely, the Freeca, has been numerically studied. The mechanism leading to the vortical flow evolution is also explained. In the flow interior, it is characterized by a large region of steady flow in the fore area, and a separated region of unsteady flow after the car. Three longitudinal vortex systems are incepted from the rear-end of the car surface, namely, the arch-type vortex, the uptilting vortex, and the long trailing vortex. The core of the vortex is seen to be in the region of high vorticity and low pressure. The fluid particles tend to be converged near the origin and diverged around the tail of the vortex coreline. Through this study, the surface streamlines on the estate car are known to have numerous topological singular points and lines of separation. The locations of the singular points and lines of separation vary with time. Several newly formed spiraling foci along the roof end, the rear-side pillars and the rear fender are seen to cause some new streamwise vortices to form. The vortices proceed downstream and undergo dissipation, cross-cancellation or entrainment into the long trailing vortex region that, altogether, form an asymmetric wake. These shedding vortices result in a vortex street behind the estate car. Furthermore, the periodically time-varying aerodynamic forces on the car body are caused by a fluctuating of flow pattern due to the alternate vortex shedding.

Acknowledgments

References

[1] R. Himeno, Car aerodynamic simulation on NEC SX-4 at Nissan research center, *SX world online magazine* No. 18, spring 1996.
[2] A. Kleber, Simulation of airflow around an Opel Astra vehicle with Fluent, *JA132*, Fluent Inc., 2001.
[3] S. Kapadia, S. Roy, and K. Wurtzler, Detached eddy simulation over a reference Ahmed car model, *AIAA-2003-0857*, 2003.
[4] Pro/ENGINEER Wildfire, Parametric Technology Corporation, 2010.
[5] ICEM-CFD, ANSYS Inc., 2010.
[6] CFX, ANSYS Inc., 2010.
[7] FIELDVIEW, Intelligent Light, 2010.
[8] B. E. Launder, G. J. Reece, and W. Rodi, Progress in the developments of a Reynolds-stress turbulence closure, *J.Fluid Mechanics*, Vol. 68, pp. 537-566, 1975.
[9] D. S. Clarke and N. S. Wilkes, The calculation of turbulent flows in complex geometries using a differential stress model, *AERE-R*, Vol. 13428, 1989.
[10] Francis T. Makowski and S. E. Kim, Advances in external-aero simulation of ground vehicles using the steady RANS equations, *SAE Paper*, 2000-01-0484, 2000.

[11] C. M. Rhie and W. L. Chow, Numerical study of the turbulent flow past an airfoil with trailing edge separation, *AIAA J1*, 21, pp. 1527-1532, 1983.

[12] S. V. Pantankar, Numerical Heat Transfer and Fluid Flow, *Hemishere Publishing co.*, 1983.

[13] D. A. Anderson and J. C. Tannehill and R. H. Pletcher, Computational Fluid Mechanics and Heat Transfer, *Hemishere Publishing co.*, 1984.

[14] B. R. Hutchinson and G. D. Raithby, A multigrid method based on the additive correction strategy, *Numerical Heat Transfer*, Vol. 9, pp. 511-537, 1986.

[15] T. Nouzawa, S. Haruna, K. Hiasa and T. Nakamura, Analysis of wake pattern for Reducing aerodynamic drag of notchback model, *SAE paper*, 900318, 1990.

[16] R. Himeno, M. Takagi, K. Fujitani and H. Tanaka, Numerical analysis of the airflow around automobile using multi-block structured grid, *SAE paper*, 900319, 1990.

[17] J. Guckenheimer and P. Holmes, Nonlinear oscillations, dynamical systems, and bifurcations of vector fields, 3rd ed., *New York:Springer-Verlag*, pp. 149-150, 1997.

[18] A. A. Sau and Robert R. Hwang and Tony W. H. Sheu and W. C. Yang, Unsteady interaction of trailing vortices in the wake of a wall-mounted rectangular block, *Physical Review E*, 68, 056303, 2003.

[19] D. Sujuki and R. Haimes, Identification of swirling flow in 3-D vector fields, *AIAA 95-1715*, 1995.

[20] R. Haimes and D. Kenwright, On the velocity gradient tensor and fluid feature extraction, *AIAA 99-3288*, 1999.